Stoichiometric Layered Potassium Transition Metal Oxide for Rechargeable Potassium Batteries

Haegyeom Kim,[†] Dong-Hwa Seo,[‡] Alexander Urban,[‡] Jinhyuk Lee,[‡] Deok-Hwang Kwon,[‡] Shou-Hang Bo,[†,§] Tan Shi,[‡] Joseph K. Papp,[∥] Bryan D. McCloskey,[∥] and Gerbrand Ceder*[,†,‡]

[†]Materials Sciences Division, Lawrence Berkeley National Laboratory, Berkeley, California 94720, United States

[‡]Department of Materials Science and Engineering, University of California, Berkeley, California 94720, United States

[§]University of Michigan−Shanghai Jiao Tong University Joint Institute, Shanghai Jiao Tong University, 800 Dong Chuan Rd., Minhang District, Shanghai 200240, People's Republic of China

[∥]Department of Chemical and Biomolecular Engineering, University of California, Berkeley, California 94720, United States

S Supporting Information

ABSTRACT: K-ion batteries are promising alternative energy storage systems for large-scale applications because of the globally abundant K reserves. K-ion batteries benefit from the lower standard redox potential of K/K^+ than that of Na/Na^+ and even Li/Li^+, which can translate into a higher working voltage. Stable KC_8 can also be formed via K intercalation into a graphite anode, which contrasts with the thermodynamically unfavorable Na intercalation into graphite, making graphite a readily available anode for K-ion battery technology. However, to construct practical rocking-chair K-ion batteries, an appropriate cathode material that can accommodate reversible K release and storage is still needed. We show that stoichiometric $KCrO_2$ with a layered O3-type structure can function as a cathode for K-ion batteries and demonstrate a practical rocking-chair K-ion battery. In situ X-ray diffraction and electrochemical titration demonstrate that K_xCrO_2 is stable for a wide K content, allowing for topotactic K extraction and reinsertion. We further explain why stoichiometric $KCrO_2$ is unique in forming the layered structure unlike other stoichiometric K-transition metal oxide compounds, which form nonlayered structures; this fundamental understanding provides insight for the future design of other layered cathodes for K-ion batteries.
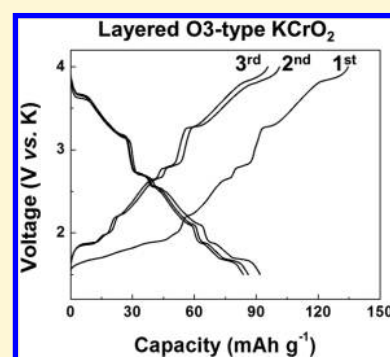
INTRODUCTION

Rechargeable batteries have emerged as an important class of technology for the storage of the intermittent energy generated from renewable resources. The use of Li-ion batteries (LIBs), which were originally commercialized to power portable electronic devices, has now expanded to large-scale applications, including electric vehicles and grids. Given the resource issues associated with Li-ion technology,[1,2] it is critical to develop alternative rechargeable battery systems. Na-ion batteries (NIBs) and K-ion batteries (KIBs) are considered promising alternatives for large-scale energy storage because of the globally abundant Na and K reserves.[3−7] KIBs are particularly interesting because of the low standard redox potential of K/K^+ compared to Na/Na^+, which can be translated into a higher working voltage. In addition, K intercalates into graphite, in contrast to Na, for which alternate anodes need to be found.[8,9]

Layered transition metal oxides (MOs) are of interest as cathode materials for LIBs and NIBs because of their high theoretical energy densities and the high respective Li and Na diffusivities in these structures.[10,11] The expectation of analogous performance in K systems has generated research interest in layered MOs as cathode materials for KIBs. Since Vaalma et al. first demonstrated that layered $K_{0.3}MnO_2$ can

reversibly cycle K,[12] several studies have investigated similar K_xMO_2 compounds, including $K_{0.7}Fe_{0.5}Mn_{0.5}O_2$,[13] K_xCoO_2 (x = 0.4 and 0.6),[14,15] $K_{0.5}MnO_2$,[8] and $K_{0.67}Ni_{0.17}Co_{0.17}Mn_{0.66}O_2$.[16] These layered materials exhibit moderate specific capacity and rate capability. However, all the layered K compounds reported to date are K-deficient phases ($K/M \leq 0.7$),[8,12−16] limiting their use in practical batteries since in a typical alkali-intercalation battery all the alkali is brought in through the cathode. Most $K-MO_2$ materials form a nonlayered structure when the K/M ratio approaches 1.0.[17−19] Therefore, there is a need to understand the fundamental factors that stabilize (or destabilize) the layered structure in $K-MO_2$ compounds and to then generalize design rules for the synthesis of new layered materials with K/M ratios near 1.0.

In the present study, we demonstrate the feasibility of using $KCrO_2$ as a KIB cathode and propose an electronic-structure mechanism that explains the stability trend of the layered KMO_2 phases (M = Sc, Ti, V, Cr, Mn, Fe, Co, and Ni). We first investigate the thermodynamic stability of layered K_xMO_2 compounds (x = 1.0) with 3d M elements from Sc to Ni using

density functional theory (DFT). Only $KScO_2$ and $KCrO_2$ were computed to be thermodynamically stable, which is consistent with the structures found in the Inorganic Crystal Structure Database (ICSD). Thus, we evaluated, for the first time, O3-type K_xCrO_2 ($x = 1$) as a positive electrode for KIBs. The $KCrO_2$ cathode delivers a specific capacity of 92 mAh g^{-1} via reversible topotactic reactions, which were confirmed by *in situ* X-ray diffraction (XRD) and electrochemical titration. This work reveals that the strong electrostatic K^+-K^+ repulsion makes layered frameworks unstable at high K concentrations (e.g., K/M = 1). However, we also show that the energy penalty resulting from these K^+-K^+ repulsions is compensated by the unusual ligand field preference of Cr^{3+} for an octahedral environment, thereby stabilizing the layered $KCrO_2$ structure.

■ EXPERIMENTAL SECTION

Synthesis of O3-Type Layered $KCrO_2$. For the synthesis of O3-type $KCrO_2$, stoichiometric amounts of KN_3 (Sigma-Aldrich), KNO_3 (Sigma-Aldrich), and Cr_2O_3 (Sigma-Aldrich) were mixed and homogenized using a planetary ball mill (Retsch PM200) at 300 rpm for 4 h. The mixed powder was pelletized and then sealed in a tightly closed steel vessel in an Ar-filled glovebox. The sample was annealed in a flow of Ar following the temperature profile in Supporting Information Figure 1. Finally, the sample was transferred into an Ar-filled glovebox to prevent contamination from moisture. Because $KCrO_2$ is air-sensitive, we handled the $KCrO_2$ compound in an Ar-filled glovebox.

Characterization of O3-Type Layered $KCrO_2$. The structure of each sample was analyzed using XRD (Rigaku Miniflex 600) with Cu Kα radiation, and the structural parameters were determined using the Rietveld method and HighScore Plus software. The sample morphologies were verified using field-emission SEM (FE-SEM; Zeiss Gemini Ultra-55). TEM samples were prepared on an ultrathin carbon grid using the drop-casting method. The preparation was conducted in a glovebox, and acetone was used as the solvent with the use of gentle sonication. EELS line profiles were obtained in scanning transmission electron microscopy (STEM)/EELS mode using a CM 200 transmission electron microscope at 200 kV. The EELS line profiles were obtained in an area in which contact between the active material and carbon was identified. For each spectrum, 0.2 eV energy dispersion was used with a time exposure of 1 s. The *in situ* XRD analysis was performed using a diffractometer equipped with a Mo source (Bruker D8) and a homemade *in situ* electrochemical cell with a Be window. The *in situ* cell was cycled galvanostatically using a potentiostat/galvanostat (Solartron 1287).

Electrochemical Measurements. Electrodes were prepared by mixing as-synthesized $KCrO_2$ (80 wt %), Super P carbon black (Timcal, 10 wt %), and PTFE (DuPont, 10 wt %) binder in an Ar-filled glovebox. Test cells were assembled into 2032 coin-cells in a glovebox with a two-electrode configuration using K-metal counter electrodes. A separator of grade GF/F (Whatman, USA) and an electrolyte of 0.7 M KPF_6 in ethylene carbonate/diethyl carbonate (EC/DEC; anhydrous, 1:1 volume ratio) were used. The electrochemical tests were performed on a battery testing station (Arbin Instruments) using cathode films with a loading density of ~5.4 mg cm^{-2}.

Gas Evolution Measurements. DEMS was used to identify and quantify the gases evolved during K extraction. The custom-built spectrometer and cell geometry used are described in detail in previous publications.[20−22] Relevant cell and device volumes were calibrated to allow for accurate measurement of the gases evolved. Electrochemical cells were prepared in a dry Ar-filled glovebox (<1 ppm of O_2 and H_2O, MBraun USA, Inc.) using a modified Swagelok design and the same materials described previously. After assembly, the cells were attached to the DEMS device and charged under a static head of positive gas pressure (~1.2 bar). At regular intervals throughout the charge, the accumulated gases were swept to the mass spectrometer chamber, and argon gas was pulled into the cell

headspace. The mass spectrometer was calibrated to determine the partial pressures of CO_2 and O_2, and the amounts of CO_2 and O_2 evolved were quantified based on the partial pressures and volume of gas swept to the mass spectrometer per pulse.

Sulfuric acid titration of the materials was performed in a small glass bulb attached to the DEMS equipment. In a glovebox, the materials were placed in the glass bulb equipped with a septum and capillaries that allowed connection to the spectrometer. After appropriately closing and capping the bulb, it was removed from the glovebox and attached to the spectrometer. Here, the DEMS setup and operation were similar to those in the electrochemical cells in that the headspace was swept from the bulb to the mass spectrometer at set intervals. After a baseline was achieved with the mass spectrometer, 1 M sulfuric acid was injected through the septum of the bulb. If carbonate was present, the immediate evolution of carbon dioxide would occur because of a reaction with the sulfuric acid.[23]

Computational Details. All the DFT calculations were performed within the *Vienna Ab Initio Simulation Package* (VASP)[24] with projector-augmented wave (PAW) pseudopotentials[25] and the SCAN meta-GGA exchange-correlation functional.[26,27] The SCAN functional has shown better predictive capability for the relative stability of various polymorphs than the conventional generalized-gradient approximation (GGA) and GGA+U approaches.[28,29] We used a kinetic energy cutoff of 520 eV and k-point meshes with a grid density of 1000 divided by the number of atoms in a unit cell. O3-$NaMO_2$ structures from the ICSD[30] were used as starting points for hypothetical O3-KMO_2. After replacing Na with K, the structures were fully relaxed with DFT/SCAN. We considered all of the stable compounds within the K−M−O composition space in the Materials Project Database[31,32] to evaluate the thermodynamic stability of the various O3-KMO_2 compounds. To compare the site preferences of Cr, Mn, Fe, Co, and Ni in the KMO_2 composition, the energies of three different K sites (octahedral, pyramidal, and tetrahedral sites) were considered. Various KMO_2 prototypes in the ICSD were considered to find the ground-state structures for each site and each compound, as tabulated in Supporting Information Table 1. All the structures were fully relaxed with DFT/SCAN.

■ RESULTS

**Thermodynamic Stability of Layered Compounds.** Figure 1 shows the calculated energy difference between the layered O3-type structure and the most stable structure for each stoichiometric KMO_2 compounds (M = Sc, Ti, V, Cr, Mn, Fe, Co, and Ni). Energies were calculated with DFT using
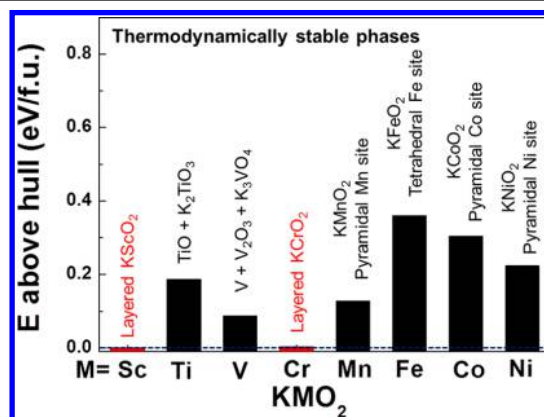
Figure 1. Thermodynamic stability of layered KMO_2 compounds. Energy above the hull for various O3-layered KMO_2 compounds. Layered $KScO_2$ and $KCrO_2$ are the only layered KMO_2 compounds that are thermodynamic ground states. All other KMO_2 compounds have a driving force (given by the height of the bar) to convert to the more stable phases listed.

the novel SCAN functional, which has recently been shown to predict ground state structures more accurately.[26−29] The results indicate that only $KScO_2$ and $KCrO_2$ are stable as layered compounds. Note that layered compounds can be categorized using an alpha-numeric expression developed by Demas et al.,[33] where the letter describes the alkali-metal site coordination by the anion as being octahedral (O) or prismatic (P) and the number indicates the periodicity of the oxygen stacking. The transition metals always occupy octahedral sites. Following this convention, the ground state of $KScO_2$ is an O3-type structure in which both Sc and K ions are situated in octahedral sites and the oxygen stacking sequence follows ABCABC. Likewise, the ground state of $KCrO_2$ is a P2-type structure in which K ions occupy prismatic sites and Cr ions occupy octahedral sites with an ABBA oxygen stacking sequence. In addition, the energy of O3-type $KCrO_2$ is only 4 meV f.u.$^{-1}$ (per formula unit of KMO_2) above that of the P2 ground state, indicating that entropy effects could stabilize the O3 structure at the synthesis temperature. In contrast, for the other M, the layered structures are more than 88 meV f.u.$^{-1}$ above their ground states, which are either a combination of compounds (for $KTiO_2$ and KVO_2) or polymorphs with different structures ($KMnO_2$, $KFeO_2$, $KCoO_2$, $KNiO_2$). For example, $KTiO_2$ favors decomposition into TiO and K_2TiO_3, and KVO_2 decomposes into V, V_2O_3, and K_3VO_3. Mn, Co, and Ni prefer to occupy pyramidal sites in the most stable $KMnO_2$, $KCoO_2$, and $KNiO_2$ phases (see Supporting Information Figure 2), respectively, whereas Fe prefers tetrahedral sites in the most stable $KFeO_2$ phase (see Supporting Information Figure 3).

Materials Characterization of $KCrO_2$. $KCrO_2$ was selected and synthesized as a cathode material for KIBs because the layered structure of $KCrO_2$ is thermodynamically stable in the stoichiometric composition from our calculations. Figure 2a presents the powder XRD refinement result for the
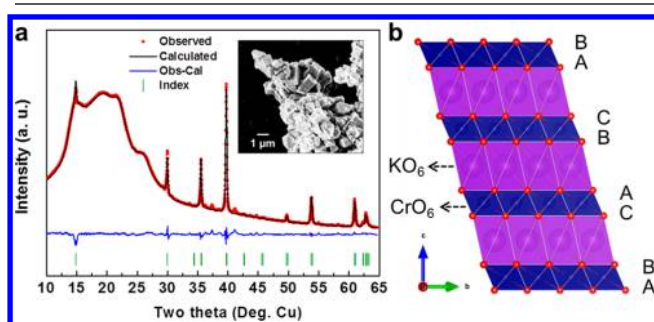
Figure 2. XRD and SEM of O3-$KCrO_2$. (a) Powder XRD refinement for the $KCrO_2$ compound (inset: SEM image). The broad background from 12° to 30° is attributed to the Kapton film used to seal the XRD sample. The refinement was performed in the $R\bar{3}m$ space group (R_{wp} = 3.16). (b) Schematic structure of O3-type $KCrO_2$.

$KCrO_2$ sample, which fits well with the $R\bar{3}m$ space group with lattice parameters of $a = b = 3.04$ Å and $c = 17.88$ Å; these results agree well with those in the literature where Delmas et al. reported the structure of O3-type $KCrO_2$.[34] This finding indicates that the prepared $KCrO_2$ sample has the O3-type ABCABC oxygen stacking sequence, wherein both Cr and K ions occupy octahedral sites, as illustrated in Figure 2b. Whereas the computed $T = 0$ K ground state of $KCrO_2$ is the P2-type phase, the experimentally synthesized phase is the O3-type structure. However, it should be noted that the slight

energy difference of ∼4 meV f.u.$^{-1}$ (P2 vs O3 structure) is well within the range of energy differences that can be overcome by entropy or stoichiometry differences between the compounds. Inductively coupled plasma mass spectrometry (ICP-MS) analysis indicates that the ratio of K/Cr is 1.02, consistent with the $KCrO_2$ composition. Scanning electron microscopy (SEM) shows a particle size of approximately 1 μm, as observed in the inset of Figure 2a. The energy-dispersive spectroscopy (EDS) mapping results reveal a uniform distribution of K, Cr, and O in the $KCrO_2$ sample (Supporting Information Figure 4).

Electrochemical K-Cycling in $KCrO_2$. To evaluate $KCrO_2$ as a cathode for KIBs, we performed galvanostatic charge/discharge measurements in a K half-cell configuration. Figure 3a presents typical capacity−voltage curves obtained at a current rate of 5 mA g^{-1}. The first charge and discharge capacities are 135 and 92 mAh g^{-1}, respectively, corresponding to the extraction of 0.63 K and the reinsertion of 0.43 K. The $KCrO_2$ cathode retains a specific discharge capacity of ∼70 mAh g^{-1} after 20 cycles at 5 mA g^{-1}, as observed in the inset of Figure 3a. Overall, the charge and discharge profiles are almost identical, indicating largely reversible K de/intercalation reactions. The position and intensity of the oxidation and reduction peaks in the dQ dV^{-1} curves in Figure 3b are well matched, consistent with reversible K extraction and insertion reactions. However, the sharp peak at ∼1.68 V (vs K/K$^+$) in the first charge (shaded red in Figure 3b) disappears in the second cycle. The stair-like voltage curves in Figure 3a and numerous dQ dV^{-1} peaks in Figure 3b indicate that multiple phase transitions occur as the K content changes.

Figure 3c shows the cycling stability of $KCrO_2$ at a current rate of 10 mA g^{-1}. The $KCrO_2$ cathode maintains a specific discharge capacity of ∼57 mAh g^{-1} (67% of the initial discharge capacity) with a Coulombic efficiency of ∼98% after 100 cycles. The rate capability was also tested, as shown in Figure 3d. Rate tests were performed after 10 cycles at a current rate of 5 mA g^{-1}. The $KCrO_2$ cathode delivers discharge capacities of 75, 65, 56, 49, 45, 40, 36, 33, and 31 mAh g^{-1} at current rates of 0.005, 0.01, 0.03, 0.05, 0.1, 0.2, 0.3, 0.4, and 0.5 A g^{-1}, respectively. To confirm the practical feasibility of a $KCrO_2$ cathode, we built a full cell with a graphite anode, and the resulting charge/discharge profile is presented in Supporting Information Figure 5. Before constructing the full cell, the graphite anode was cycled at 0.005−1.5 V (vs K/K$^+$) in a half-cell configuration to overcome the large irreversible capacity in the first cycle.[14] The full cell delivers a charge capacity of ∼97 mAh g^{-1} and a reversible discharge capacity of ∼82 mAh g^{-1} in the second cycle. The specific capacity is calculated based on only the weight of the $KCrO_2$ cathode material.

Structure Evolution of $KCrO_2$ during Charge and Discharge. Figure 4a presents typical charge/discharge profiles of a $KCrO_2$ cathode obtained at a current rate of 2 mA g^{-1}, and Figure 4b shows the corresponding in situ XRD patterns. Figure 4c and d magnify the highlighted regions in Figure 4b. As observed in the in situ XRD patterns in Figure 4c, the (006) peak near 13° moves to lower angles during charge as the increased repulsion between oxygen atoms increases the interslab distance upon K extraction, similar to observations in other layered compounds.[8,14,15] Figure 4d marks the series of phase transitions occurring as the K content changes. The multitude of distinct phases formed is consistent with the stair-like charge profile observed in Figure 3a. At the beginning of charge, the (104) peak splits into (20−2) and (111) peaks
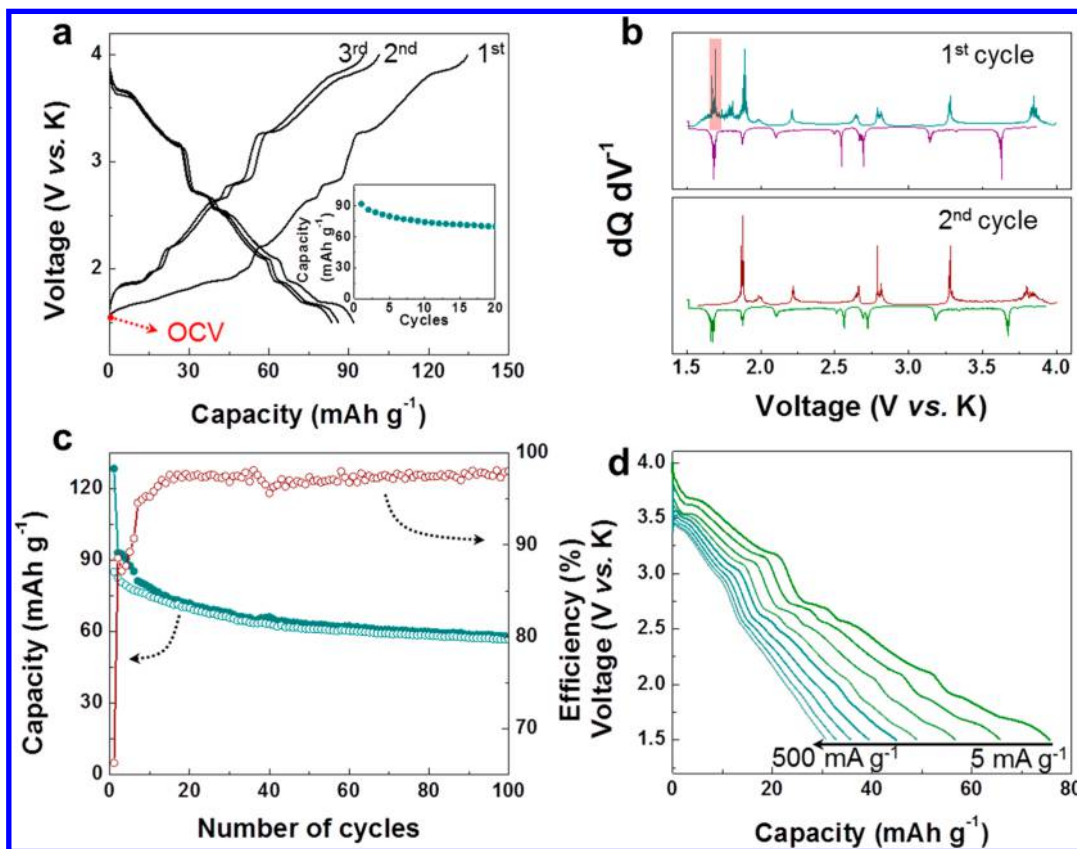
Figure 3. K-storage properties of KCrO$_2$ in K cells. (a) Typical voltage−capacity curves at a current rate of 5 mA g^{-1} (inset: cycle stability). (b) dQ dV^{-1} vs voltage curves. (c) Cycle stability of KCrO$_2$ at a current rate of 10 mA g^{-1}. (d) Discharge profiles at current rates from 0.005 to 0.5 A g^{-1}.
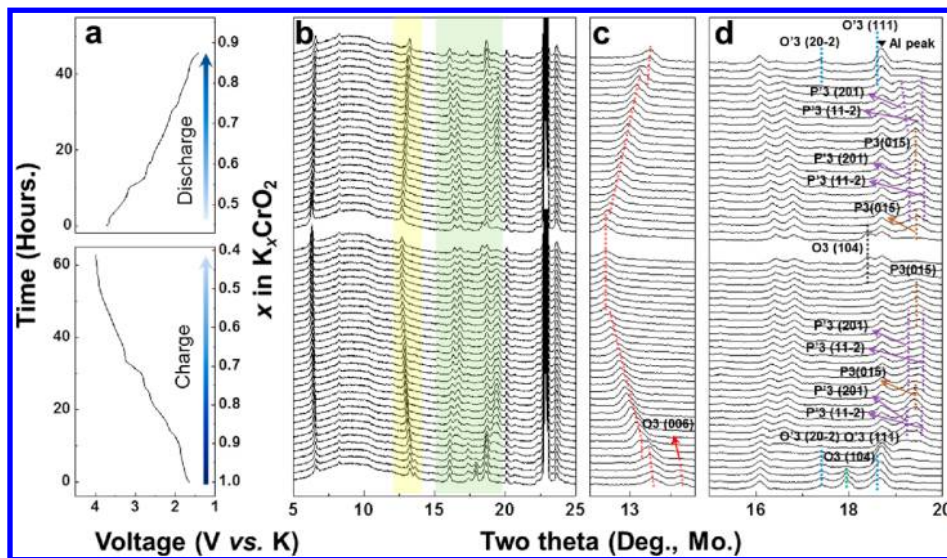
Figure 4. *In situ* XRD characterization of KCrO$_2$. (a) Typical voltage−time curves at a current rate of 2 mA g^{-1}. (b) *In situ* XRD patterns of KCrO$_2$ between 5° and 25°. (c,d) XRD patterns of highlighted regions (c, yellow; d, green) in b.

with the simultaneous appearance of a new peak at ∼13.2° at the expense of the (006) peak for 1.0 > x > 0.92 in K$_x$CrO$_2$. This result suggests the occurrence of an O3−O′3 transition (the ′ indicates monoclinic distortion). For 0.92 > x > 0.82 in K$_x$CrO$_2$, a new set of (201) and (11−2) peaks evolve at ∼19.5°, and a new peak appears at ∼13.1° at the expense of the peak at ∼13.2°, indicative of an O′3−P′3 phase transition. Then, the (201) and (11−2) peaks merge into the (015) peak via continuous K extractions at x ∼ 0.78 in K$_x$CrO$_2$, giving rise

to the P′3−P3 transition. The peak at ∼13° does not exhibit the characteristic splitting of a two-phase reaction, possibly because of the limited resolution of the laboratory XRD measurements. The (015) peak then splits into (201)/(11−2) again, indicative of the P3−P′3 transition, for 0.78 > x > 0.58 in K$_x$CrO$_2$. For 0.58 > x > 0.48 in K$_x$CrO$_2$, the (201) and (11−2) peaks merge into the (015) peak of the P3 phase. Finally, for 0.48 > x > 0.43 in K$_x$CrO$_2$, a new (104) peak appears at ∼18.4° while the intensity of the (015) peak at ∼19.5°
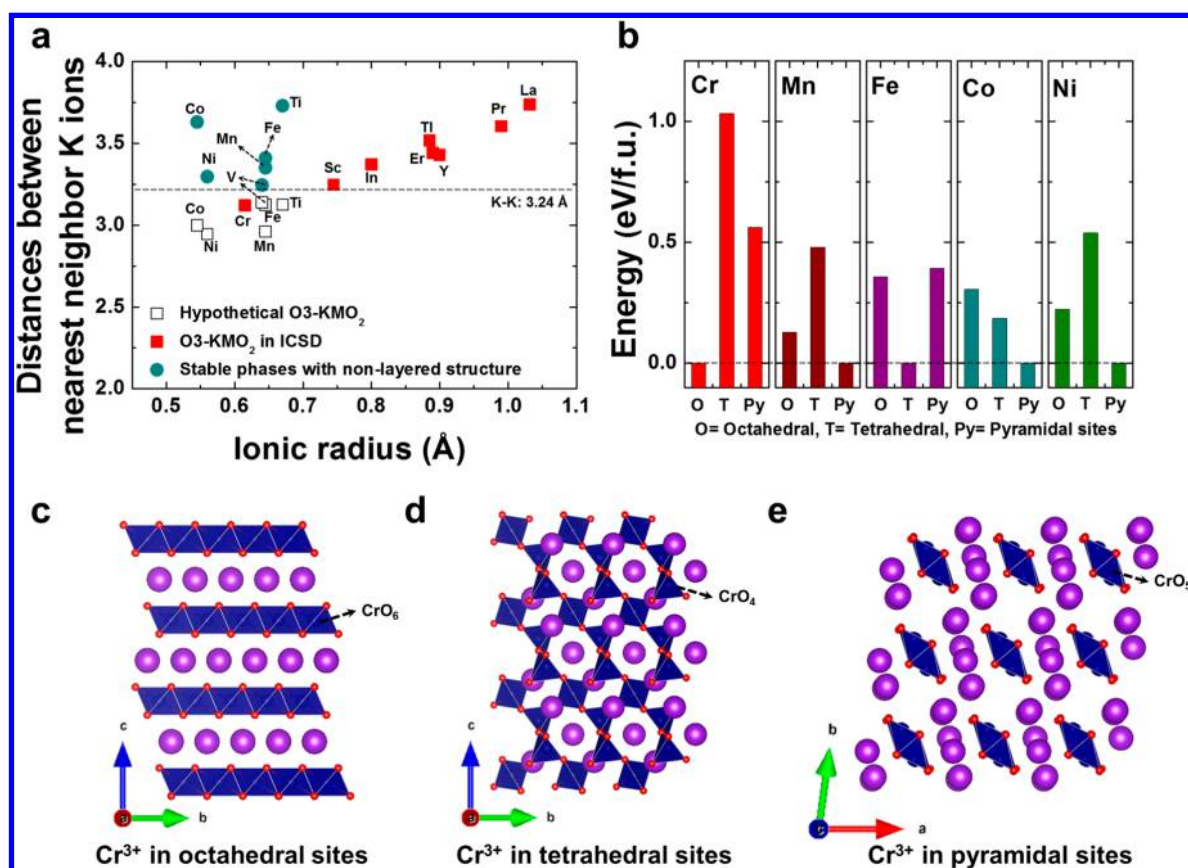
Figure 5. Distance between nearest-neighbor K ions and site preference of metals in KMO_2. (a) Plots of distance between nearest-neighbor K ions vs ionic radius of metals in KMO_2. The open and filled squares are unstable (hypothetic) and stable (reported in the ICSD) compounds with layered structures. The filled circles are the stable compounds with nonlayered structures. (b) Site preference energy of Cr, Mn, Fe, Co, and Ni in the KMO_2 composition. The crystal structure of stable $KCrO_2$ compounds when Cr^{3+} occupies (c) octahedral, (d) tetrahedral, and (e) pyramidal sites.

diminishes, which is a fingerprint of the P3−O3 transition. It should be noted that the O3 (O′3) and P3 (P′3) phases have different K sites, with K ions occupying octahedral and prismatic sites in the O3 (O′3) and P3 (P′3) phases, respectively. These layered structures can be transformed into each other via sliding of the CrO_2 slabs without breaking Cr−O bonds. The O3−O′3−P′3−P3−P′3−P3−O3 sequence of phases that O3-type K_xCrO_2 goes through when K is removed is more complicated than what occurs when O3-type Na_xCrO_2 is desodiated: O3-Na_xCrO_2 transforms to O′3 Na_xCrO_2 when $0.92 > x > 0.7$ which then further converts to P′3 Na_xCrO_2 for $0.7 > x > 0.5$.[35] The stronger and more numerous phase transition in K_xCrO_2 are likely attributable to the strong $K^+−K^+$ interaction, which leads to many intermediate phases in order to minimize $K^+−K^+$ interaction as a function of K content. The K reinsertion follows the opposite path of K extraction, indicating reversible reactions. However, the O′3 structure is not converted into the O3 structure even at the end of discharge, which suggests that the K_xCrO_2 material cannot fully reintercalate K ions upon discharge in our *in situ* experiments. We expect that the sluggish kinetics of K ions when $x \sim 1$ in K_xCrO_2 is most likely responsible for the difficulty of achieving full K-ion reinsertion in K_xCrO_2.

We observed that the $KCrO_2$ electrode has undergone some reaction even before performing the *in situ* experiments. The close-up in Figure 4c shows that two peaks are present near 13.5°, which may correspond to (00l), and in Figure 4d two

additional peaks are observed near the (104) peak of $KCrO_2$ at 18° To understand possible phase separation in the electrode material before cycling, we performed additional XRD experiments (Supporting Information Figure 6). For the electrode prepared with carbon and polytetrafluoroethylene (PTFE) binder, the reaction of $KCrO_2$ is detectable (see shaded regions of Supporting Information Figure 6), and the intensity of the newly evolved peaks increases with increasing carbon content. In contrast, no evidence of phase separation was detected for the electrode without carbon. The newly appearing peaks match well with the peaks of depotassiated K_xCrO_2, which suggests that K ions are partially extracted from $KCrO_2$ when the material is in contact with carbon. The transmission electron microscopy (TEM) image of a $KCrO_2$ particle embedded in the carbon matrix material of the electrode and corresponding electron energy loss spectroscopy (EELS) profiles in Supporting Information Figure 7 provide further evidence of the presence of K ions in the carbon material in contact with $KCrO_2$ particles. Therefore, we expect that K ions are partially extracted from $KCrO_2$ and then transferred to the carbon in the electrode, resulting in the observed reactivity of $KCrO_2$ before running the cell *in situ*. However, at an open-circuit voltage (OCV) of ~1.5 V, potassium intercalation into carbon is unlikely. Instead, it is possible that functional groups on the carbon surface store K ions.[36]

Supporting Information Figure 8a shows the overcharge behavior of the $KCrO_2$ cathode. When $KCrO_2$ is charged to 4.5 V (vs K/K^+), another plateau near 4.3 V is observed in the voltage profile, and the subsequent charge/discharge profiles become plateau-less, indicating the occurrence of an irreversible structural change during the charge process to 4.5 V (vs K/K^+). To understand this phenomenon, we conducted *ex situ* XRD measurements (Supporting Information Figure 8b). As observed in Supporting Information Figure 8b, the XRD patterns of the $KCrO_2$ electrode are no longer characteristic of those of layered oxide compounds and instead reflect the presence of an amorphous-like phase after charging to 4.5 V (vs K/K^+) without recovery even after subsequent discharge to 1.5 V (vs K/K^+).

■ DISCUSSION

Many Li- and Na-layered MOs are stable at an alkali metal//M ratio of 1 (Li/M and Na/M = 1).[37−40] However, in previously reported layered $K-MO_2$ compounds, the K/M ratio is less than 0.7.[8,12−16] We investigated stable K-layered compounds to understand why layered K-MOs usually have K-deficient compositions unlike their Li and Na analogues. Figure 5a presents a plot of the distance between nearest-neighbor K ions vs the ionic radius of Ms in layered-KMO_2 compounds. We also evaluated various stoichiometric KMO_2 (K/M/O = 1/1/2) compounds in the ICSD[30] and added the ground states of those compounds to the plot in Figure 5a. In O3-type layered compounds, the K^+−K^+ distance is set by the size of the M, as this partly controls the *a* lattice parameter. Therefore, large cations (e.g., Sc, In, Er, Tl, Y, Pr, and La) can accommodate a reasonable K^+−K^+ distance, thereby stabilizing O3-type layered structures, as shown in Figure 5a. In contrast, small Ms such as Ti, V, Mn, Fe, Co, and Ni destabilize the layered structure as their O3-KMO_2 cannot accommodate a reasonable K^+−K^+ distance, resulting from stronger electrostatic repulsion between K ions. Instead, nonlayered structures are formed for the small Ms, for which much longer K^+−K^+ distances are observed compared with those in their layered counterparts, as shown in Figure 5a. Interestingly, in these nonlayered structures, the M ions typically occupy nonoctahedral sites. For example, Mn, Co, and Ni sit at pyramidal sites in the most stable $KMnO_2$, $KCoO_2$, and $KNiO_2$ phases, respectively, and Fe occupies tetrahedral sites in the most stable $KFeO_2$ phase (Figure 1 and Supporting Information Figures S2 and S3). These structures offer more space for K ions and thus lead to longer K^+−K^+ distances than the O3-layered structure.

The most interesting observation is that $KCrO_2$ has a stable O3-type layered structure despite the relatively small ionic size of Cr^{3+}. We calculated and compared the energies of KMO_2 compounds (M = Cr, Mn, Fe, Co, and Ni) when M^{3+} occupies octahedral, tetrahedral, and pyramidal sites in the given ground states to investigate the relative site preference of Ms, as shown in Figure 5b−e. For $KCrO_2$, the structure in which Cr^{3+} sits at octahedral sites is more stable than for the other structures by >0.5 eV f.u.$^{-1}$, indicating that Cr^{3+} strongly prefers occupying octahedral sites rather than tetrahedral or pyramidal sites despite the strong repulsion between K ions. This preference is due to the unusual ligand field preference of Cr^{3+} for the octahedral environment, which compensates for the energy penalty from the short K^+−K^+ distance.[41−43] In contrast, other small Ms, including Mn, Fe, Co, and Ni, occupy tetrahedral or pyramidal sites in the ground states. In ligand field theory, 3d orbitals are split depending on the M site significantly

(Supporting Information Figure 9).[41,42,44] For example, 3d orbitals are separated into two higher-energy e_g and three lower-energy t_{2g} orbitals for octahedrally coordinated M but are split into b_{1g}, a_{1g}, b_{2g}, and e_g orbitals when M occupies a pyramidal site. The d^3 electron configuration of Cr^{3+} highly prefers octahedral sites. In contrast, Mn^{3+} with d^4 can be stabilized in pyramidal sites, and Fe^{3+} with d^5 occupancy becomes stabilized in the tetrahedral coordination. Notably, Co^{3+} also has a very high octahedral ligand field stabilization; however, its extremely small ionic radius compared with that of Cr^{3+} would result in such short K^+−K^+ distances that the energetic penalty from K^+−K^+ repulsion outweighs the stabilization provided by octahedral coordination of O around Co^{3+}.

Supporting Information Figure 8 demonstrates that K_xCrO_2 becomes amorphous at low K concentrations ($x < 0.35$). However, entirely different behavior has been reported for its Na analogue, $NaCrO_2$, for which crystalline rock-salt CrO_2 is formed when more than 0.6 Na ions are extracted.[40] The desodiation of more than 0.6 Na ions from $NaCrO_2$ leads to the charge disproportionation of Cr^{4+} into Cr^{3+} and Cr^{6+}. It has been suggested that the resulting small Cr^{6+} cations migrate into intermediate tetrahedral sites in the Na layers. The Cr^{6+} cations in the tetrahedral sites undergo a subsequent comproportionation with neighboring Cr^{3+} cations, forming Cr^{4+}. The resulting Cr^{4+} cations likely migrate into octahedral sites in the Na layers, generating the rock-salt CrO_2 structure. However, in $KCrO_2$, several factors may favor amorphization. Cr^{6+} migration into the intermediate tetrahedral sites in the K layers is less favorable because of the larger K slab spacing that creates highly distorted sites in the K layers. This structural effect makes Cr^{6+} migration in the K layers less favorable than in $NaCrO_2$. In addition, as Cr^{3+} is oxidized, some of the strong ligand field stabilization for the octahedral site is removed, creating a large driving force for a collapse of the structure. In addition, the large size difference of Cr^{6+} and Cr^{3+} in the Cr layers can lead to mechanical stress, resulting in a crystalline-to-amorphous transition when the stress is accumulated, as often observed in metal oxides and silicon.[45−47]

One may expect oxygen evolution to occur at high voltages in $KCrO_2$ similar to some Li and Na cathode materials that release lattice oxygen as part of irreversible phase transformation at high voltage.[48−50] We performed differential electrochemical mass spectrometry (DEMS) analysis of the first K extraction cycle of the $KCrO_2$ material (Supporting Information Figure 10), and no observable O_2 evolution was detected. However, a significant amount of CO_2 evolves upon charge above 3.5 V, which can be attributed to electrolyte decomposition for the following reasons: Substantial anodic currents at >3.5 V (vs K/K^+) are observed in a linear sweep voltammetry (LSV) measurement (Supporting Information Figure 11). These currents likely result from parasitic electrochemical reactions involving electrolyte decomposition, although further studies are needed to confirm this assertion. CO_2 can also evolve from impurities such as solid carbonates on the surface of the electrode that arise during synthesis and handling procedures.[23,51] However, a carbonate titration experiment[23] (see Experimental Section and Supporting Information Figure 12) indicates that little solid carbonate is present on our as-prepared material surfaces and that roughly 500 times more CO_2 is evolved during the first charge than surface carbonate initially present in the electrode. These

combined data strongly suggest that the CO_2 evolution results from electrolyte decomposition.

CONCLUSION

We demonstrated that layered O3-type $KCrO_2$ can function as a cathode material for KIBs and used it in a full-cell KIB with a graphite anode. To the best of our knowledge, this work represents the first demonstration of reversible K extraction/reinsertion in O3-type layered $KCrO_2$ via a topotactic reaction. The $KCrO_2$ cathode delivers a reversible capacity of ~90 mAh g^{-1} with an average redox potential of ~2.73 V (vs K/K$^+$). In addition, $KCrO_2$ exhibits good cycle stability and rate capability, indicating that the KIB system could be an effective technology for large-scale energy storage. Our understanding of how the stoichiometric $KCrO_2$ is stabilized in the layered structure (unlike for other transition metal oxide compounds) provides insight for the design of other layered oxide cathode materials for K-ion batteries.

ASSOCIATED CONTENT

Ⓢ Supporting Information

The Supporting Information is available free of charge on the ACS Publications website at DOI: 10.1021/acs.chemmater.8b03228.

Structure of nonlayered KMO_2, SEM-EDS, charge/discharge profile of $KCrO_2$/graphite full cell, XRD of $KCrO_2$ electrode prepared with PTFE and carbon, TEM-EELS, charge/discharge profile of $KCrO_2$ between 4.5 and 1.5 V, ex-situ XRD, energy level diagrams for 3d orbitals of transition metals, gas evolution measurements, linear sweep voltammetry of the electrolyte (PDF)

AUTHOR INFORMATION

Corresponding Author

*E-mail: gceder@berkeley.edu.

ORCID Ⓖ

Haegyeom Kim: 0000-0002-5962-8244
Tan Shi: 0000-0003-0312-2639
Joseph K. Papp: 0000-0002-7982-6096
Bryan D. McCloskey: 0000-0001-6599-2336

Author Contributions

H.K. designed and conducted experiments, and G.C. guided experiments. H.K. and G.C. wrote the manuscript, and all the authors reviewed the manuscript. D.-H.S. conducted DFT calculations. H.K., A.U., J.L., S.-H.B., and G.C. discussed the experiment and calculation results. T.S. conducted SEM experiments, and D.-H.K. conducted TEM experiments. J.K.P. conducted gas evolution measurements. H.K., B.D.M., and J.K.P. discussed the gas evolution experiment results. All authors have given approval to the final version of the manuscript.

Notes

The authors declare no competing financial interest.

ACKNOWLEDGMENTS

REFERENCES

(1) Kim, H.; Kim, H.; Ding, Z.; Lee, M. H.; Lim, K.; Yoon, G.; Kang, K. Recent Progress in Electrode Materials for Sodium-Ion Batteries. *Adv. Energy. Mater.* **2016**, *6*, 1600943.

(2) Olivetti, E. A.; Ceder, G.; Gaustad, G. G.; Fu, X. Lithium-Ion Battery Supply Chain Considerations: Analysis of Potential Bottlenecks in Critical Metals. *Joule* **2017**, *1*, 229−243.

(3) Kim, S.-W.; Seo, D.-H.; Ma, X.; Ceder, G.; Kang, K. Electrode Materials for Rechargeable Sodium-Ion Batteries: Potential Alternatives to Current Lithium-Ion Batteries. *Adv. Energy. Mater.* **2012**, *2*, 710−721.

(4) Eftekhari, A.; Jian, Z.; Ji, X. Potassium Secondary Batteries. *ACS Appl. Mater. Interfaces* **2017**, *9*, 4404−4419.

(5) Pramudita, J. C.; Sehrawat, D.; Goonetilleke, D.; Sharma, N. An Initial Review of the Status of Electrode Materials for Potassium-Ion Batteries. *Adv. Energy. Mater.* **2017**, *7*, 1602911.

(6) Wu, X.; Leonard, D. P.; Ji, X. Emerging Non-Aqueous Potassium-Ion Batteries: Challenges and Opportunities. *Chem. Mater.* **2017**, *29*, 5031−5042.

(7) Zou, X.; Xiong, P.; Zhao, J.; Hu, J.; Liu, Z.; Xu, Y. Recent research progress in non-aqueous potassium-ion batteries. *Phys. Chem. Chem. Phys.* **2017**, *19*, 26495−26506.

(8) Kim, H.; Seo, D.-H.; Kim, J. C.; Bo, S.-H.; Liu, L.; Shi, T.; Ceder, G. Investigation of Potassium Storage in Layered P3-Type K0.5MnO2 Cathode. *Adv. Mater.* **2017**, *29*, 1702480.

(9) Komaba, S.; Hasegawa, T.; Dahbi, M.; Kubota, K. Potassium intercalation into graphite to realize high-voltage/high-power potassium-ion batteries and potassium-ion capacitors. *Electrochem. Commun.* **2015**, *60*, 172−175.

(10) He, P.; Yu, H.; Li, D.; Zhou, H. Layered lithium transition metal oxide cathodes towards high energy lithium-ion batteries. *J. Mater. Chem.* **2012**, *22*, 3680−3695.

(11) Han, M. H.; Gonzalo, E.; Singh, G.; Rojo, T. A comprehensive review of sodium layered oxides: powerful cathodes for Na-ion batteries. *Energy Environ. Sci.* **2015**, *8*, 81−102.

(12) Vaalma, C.; Giffin, G. A.; Buchholz, D.; Passerini, S. Non-Aqueous K-Ion Battery Based on Layered K0.3MnO2 and Hard Carbon/Carbon Black. *J. Electrochem. Soc.* **2016**, *163*, A1295−A1299.

(13) Wang, X.; Xu, X.; Niu, C.; Meng, J.; Huang, M.; Liu, X.; Liu, Z.; Mai, L. Earth Abundant Fe/Mn-Based Layered Oxide Interconnected Nanowires for Advanced K-Ion Full Batteries. *Nano Lett.* **2017**, *17*, 544−550.

(14) Kim, H.; Kim, J. C.; Bo, S.-H.; Shi, T.; Kwon, D.-H.; Ceder, G. K-Ion Batteries Based on a P2-Type K0.6CoO2 Cathode. *Adv. Energy. Mater.* **2017**, *7*, 1700098.

(15) Hironaka, Y.; Kubota, K.; Komaba, S. P2- and P3-KxCoO2 as an electrochemical potassium intercalation host. *Chem. Commun.* **2017**, *53*, 3693−3696.

(16) Liu, C.; Luo, S.; Huang, H.; Wang, Z.; Hao, A.; Zhai, Y.; Wang, Z. K0.67Ni0.17Co0.17Mn0.66O2: A cathode material for potassium-ion battery. *Electrochem. Commun.* **2017**, *82*, 150−154.

(17) Jansen, M.; Chang, F. M.; Hoppe, R. Zur Kenntnis von KMnO2. *Z. Anorg. Allg. Chem.* **1982**, *490*, 101−110.

(18) Ali, N. Z.; Nuss, J.; Sheptyakov, D.; Jansen, M. The AFeO2 (A = K, Rb and Cs) family: A comparative study of structures and structural phase transitions. *J. Solid State Chem.* **2010**, *183*, 752−759.

(19) Jansen, M.; Hoppe, R. Zur Kenntnis von KCoO2 und RbCoO2. *Z. Anorg. Allg. Chem.* **1975**, *417*, 31−34.

(20) McCloskey, B. D.; Bethune, D. S.; Shelby, R. M.; Girishkumar, G.; Luntz, A. C. Solvents' Critical Role in Nonaqueous Lithium−Oxygen Battery Electrochemistry. *J. Phys. Chem. Lett.* **2011**, *2*, 1161−1166.

(21) McCloskey, B. D.; Scheffler, R.; Speidel, A.; Bethune, D. S.; Shelby, R. M.; Luntz, A. C. On the Efficacy of Electrocatalysis in Nonaqueous Li−O2 Batteries. *J. Am. Chem. Soc.* **2011**, *133*, 18038−18041.

(22) McCloskey, B. D.; Speidel, A.; Scheffler, R.; Miller, D. C.; Viswanathan, V.; Hummelshøj, J. S.; Nørskov, J. K.; Luntz, A. C. Twin Problems of Interfacial Carbonate Formation in Nonaqueous Li−O2 Batteries. *J. Phys. Chem. Lett.* **2012**, *3*, 997−1001.

(23) Renfrew, S. E.; McCloskey, B. D. Residual lithium carbonate predominantly accounts for first cycle CO2 and CO outgassing of Li-stoichiometric and Li-rich layered transition metal oxides. *J. Am. Chem. Soc.* **2017**, *139*, 17853−17860.

(24) Kresse, G.; Furthmüller, J. Efficiency of ab-initio total energy calculations for metals and semiconductors using a plane-wave basis set. *Comput. Mater. Sci.* **1996**, *6*, 15−50.

(25) Blöchl, P. E. Projector augmented-wave method. *Phys. Rev. B: Condens. Matter Mater. Phys.* **1994**, *50*, 17953−17979.

(26) Sun, J.; Ruzsinszky, A.; Perdew, J. P. Strongly Constrained and Appropriately Normed Semilocal Density Functional. *Phys. Rev. Lett.* **2015**, *115*, 036402.

(27) Sun, J.; Remsing, R. C.; Zhang, Y.; Sun, Z.; Ruzsinszky, A.; Peng, H.; Yang, Z.; Paul, A.; Waghmare, U.; Wu, X.; Klein, M. L.; Perdew, J. P. Accurate first-principles structures and energies of diversely bonded systems from an efficient density functional. *Nat. Chem.* **2016**, *8*, 831−836.

(28) Kitchaev, D. A.; Peng, H.; Liu, Y.; Sun, J.; Perdew, J. P.; Ceder, G. Energetics of MnO2 polymorphs in density functional theory. *Phys. Rev. B: Condens. Matter Mater. Phys.* **2016**, *93*, 045132.

(29) Kitchaev, D. A.; Dacek, S. T.; Sun, W.; Ceder, G. Thermodynamics of Phase Selection in MnO2 Framework Structures through Alkali Intercalation and Hydration. *J. Am. Chem. Soc.* **2017**, *139*, 2672−2681.

(30) Inorganic Crystal Structure Database (ICSD). http://icsdweb.fiz-karlsruhe.de (accessed May 15, 2017).

(31) Jain, A.; Ong, S. P.; Hautier, G.; Chen, W.; Richards, W. D.; Dacek, S.; Cholia, S.; Gunter, D.; Skinner, D.; Ceder, G.; Persson, K. A. Commentary: The Materials Project: A materials genome approach to accelerating materials innovation. *APL Mater.* **2013**, *1*, 011002.

(32) Ong, S. P.; Cholia, S.; Jain, A.; Brafman, M.; Gunter, D.; Ceder, G.; Persson, K. A. The Materials Application Programming Interface (API): A simple, flexible and efficient API for materials data based on REpresentational State Transfer (REST) principles. *Comput. Mater. Sci.* **2015**, *97*, 209−215.

(33) Delmas, C.; Fouassier, C.; Hagenmuller, P. Structural classification and properties of the layered oxides. *Physica B+C* **1980**, *99*, 81−85.

(34) Delmas, C.; Devalette, M.; Fouassier, C.; Hagenmuller, P. Les phases KXCrO2 (X ≤ 1). *Mater. Res. Bull.* **1975**, *10*, 393−398.

(35) Zhou, Y.-N.; Ding, J.-J.; Nam, K.-W.; Yu, X.; Bak, S.-M.; Hu, E.; Liu, J.; Bai, J.; Li, H.; Fu, Z.-W.; Yang, X.-Q. Phase transition behavior of NaCrO2 during sodium extraction studied by synchrotron-based X-ray diffraction and absorption spectroscopy. *J. Mater. Chem. A* **2013**, *1*, 11130−11134.

(36) Kim, H.; Lim, H.-D.; Kim, S.-W.; Hong, J.; Seo, D.-H.; Kim, D.-c.; Jeon, S.; Park, S.; Kang, K. Scalable Functionalized Graphene Nano-platelets as Tunable Cathodes for High-performance Lithium Rechargeable Batteries. *Sci. Rep.* **2013**, *3*, 1506.

(37) Ohzuku, T.; Ueda, A. Solid-State Redox Reactions of LiCoO2 (R3̄m) for 4 V Secondary Lithium Cells. *J. Electrochem. Soc.* **1994**, *141*, 2972−2977.

(38) Liu, W.; Oh, P.; Liu, X.; Lee, M.-J.; Cho, W.; Chae, S.; Kim, Y.; Cho, J. Nickel-Rich Layered Lithium Transition-Metal Oxide for High-Energy Lithium-Ion Batteries. *Angew. Chem., Int. Ed.* **2015**, *54*, 4440−4457.

(39) Ma, X.; Chen, H.; Ceder, G. Electrochemical Properties of Monoclinic NaMnO2. *J. Electrochem. Soc.* **2011**, *158*, A1307−A1312.

(40) Bo, S.-H.; Li, X.; Toumar, A. J.; Ceder, G. Layered-to-Rock-Salt Transformation in Desodiated NaxCrO2 (x 0.4). *Chem. Mater.* **2016**, *28*, 1419−1429.

(41) Dunitz, J. D.; Orgel, L. E. Electronic properties of transition-metal oxides-II: Cation distribution amongst octahedral and tetrahedral sites. *J. Phys. Chem. Solids* **1957**, *3*, 318−323.

(42) Burns, R. G. Site preferences of transition metal ions in silicate crystal structures. *Chem. Geol.* **1970**, *5*, 275−283.

(43) Reed, J.; Ceder, G. Role of Electronic Structure in the Susceptibility of Metastable Transition-Metal Oxide Structures to Transformation. *Chem. Rev.* **2004**, *104*, 4513−4534.

(44) Das, T.; Nicholas, J. D.; Qi, Y. Long-range charge transfer and oxygen vacancy interactions in strontium ferrite. *J. Mater. Chem. A* **2017**, *5*, 4493−4506.

(45) Dhawan, S.; Dhawan, T.; Vedeshwar, A. G. Crystalline to amorphous phase transformation of Ta2O5 quantum dots driven by residual stress. *J. Alloys Compd.* **2016**, *657*, 366−371.

(46) Dhawan, S.; Dhawan, T.; Vedeshwar, A. G. Residual stress induced crystalline to amorphous phase transformation in Nb2O5 quantum dots. *J. Appl. Phys.* **2014**, *116*, 043503.

(47) Wang, Y.-C.; Zhang, W.; Wang, L.-Y.; Zhuang, Z.; Ma, E.; Li, J.; Shan, Z.-W. In situ TEM study of deformation-induced crystalline-to-amorphous transition in silicon. *NPG Asia Mater.* **2016**, *8*, e291.

(48) Hong, J.; Lim, H.-D.; Lee, M.; Kim, S.-W.; Kim, H.; Oh, S.-T.; Chung, G.-C.; Kang, K. Critical Role of Oxygen Evolved from Layered Li−Excess Metal Oxides in Lithium Rechargeable Batteries. *Chem. Mater.* **2012**, *24*, 2692−2697.

(49) Armstrong, A. R.; Holzapfel, M.; Novák, P.; Johnson, C. S.; Kang, S.-H.; Thackeray, M. M.; Bruce, P. G. Demonstrating Oxygen Loss and Associated Structural Reorganization in the Lithium Battery Cathode Li[Ni0.2Li0.2Mn0.6]O2. *J. Am. Chem. Soc.* **2006**, *128*, 8694−8698.

(50) Lee, J.; Papp, J. K.; Clément, R. J.; Sallis, S.; Kwon, D.-H.; Shi, T.; Yang, W.; McCloskey, B. D.; Ceder, G. Mitigating oxygen loss to improve the cycling performance of high capacity cation-disordered cathode materials. *Nat. Commun.* **2017**, *8*, 981.

(51) Renfrew, S. E.; McCloskey, B. D. High Voltage Behavior of Ni-Rich Li(NixMnyCoz)O2 Cathodes in Li-Ion Batteries. *ECS Meeting Abstract*; The Electrochemical Society, 2017; p 372.